pH-dependent molecular dynamics of vesicular stomatitis virus glycoprotein G

Pia Rücker,[1] Silke A. Wieninger,[2] G. Matthias Ullmann,[2] and Heinrich Sticht[1]*

[1] Bioinformatics, Institute of Biochemistry, Friedrich-Alexander-Universität Erlangen-Nürnberg, 91054 Erlangen, Germany

[2] Computational Biochemistry/Bioinformatics, University of Bayreuth, 95447 Bayreuth, Germany

ABSTRACT

Vesicular stomatitis virus glycoprotein G (VSV-G) belongs to a new class of viral fusion proteins (Class III). The structure of VSV-G has been solved in two different conformations and fusion is known to be triggered by low pH. To investigate Class III fusion mechanisms, molecular dynamics simulations were performed on the VSV-G prefusion structure in two different protonation states: at physiological pH (pH 7) and low pH present in the endosome (pH 5). Domain IV containing the fusion loops, which need to interact with the target membrane, exhibits the highest mobility. Energetic analyses revealed weakened interaction between Domain IV and the protein core at pH 5, which can be attributed to two pairs of structurally neighboring conserved and differentially protonated residues in the Domain IV–core interface. Energetic calculations also demonstrated that the interaction between the subunits in the core of the trimeric VSV-G is strengthened at pH 5, mainly due to newly formed interactions between the C-terminal loop of Domain II and the N-terminus of the adjacent subunit. A pair of interacting residues in this interface that is affected by differential protonation was shown to be the main effectors of this phenomenon. The results of this study thus enhance the mechanistic understanding of the effects of protonation changes in VSV-G.

INTRODUCTION

For coated viruses, fusion of the virus membrane with the host cell membrane is a prerequisite for genome release and reproduction of virus particles. Viral entry can be triggered under neutral pH conditions on the plasma membrane by receptor interaction or can occur under mildly acidic conditions from the inside of endosomes after endocytosis of the particle.[1,2] Members of the rhabdovirus family have only one surface glycoprotein, glycoprotein G, representing the sole fusion mediator[3,4] and take advantage of the low pH conditions in the late endosome to induce membrane fusion.[3] A new class (Class III[5,6]) of viral fusion proteins has recently been defined based on the structure of vesicular stomatitis virus glycoprotein G (VSV-G). This protein is trimeric, contains internal fusion loops, and its fusion capacity has been shown to be pH dependent.[7–11]

Membrane fusion is triggered during the transition from the high- to low-pH form, which were termed VSV-G prefusion and postfusion conformation, respectively. Determination of the crystal structure of VSV-G at two different pH values[12,13] revealed considerable differences in the do-main arrangement, indicating that large-scale structural rearrangements occur during the fusion process [Fig. 1(A,B)]. The prefusion structure is rather compact with the extended Domain IV, which contains the fusion loops, oriented toward the virus membrane [Fig. 1(A)]. For the fusion loops to contact the host cell membrane and induce membrane fusion [Fig. 1(A), cyan arrow], unlocking of Domain IV from this position appears necessary.

As the pH optimum of fusion is between 5 and 6, histidine residues have been suggested to be involved in the molecular switches triggering conformational change of the glycoprotein and subsequent membrane fusion[14]; however, the mechanistic role of individual histidines still needs to be
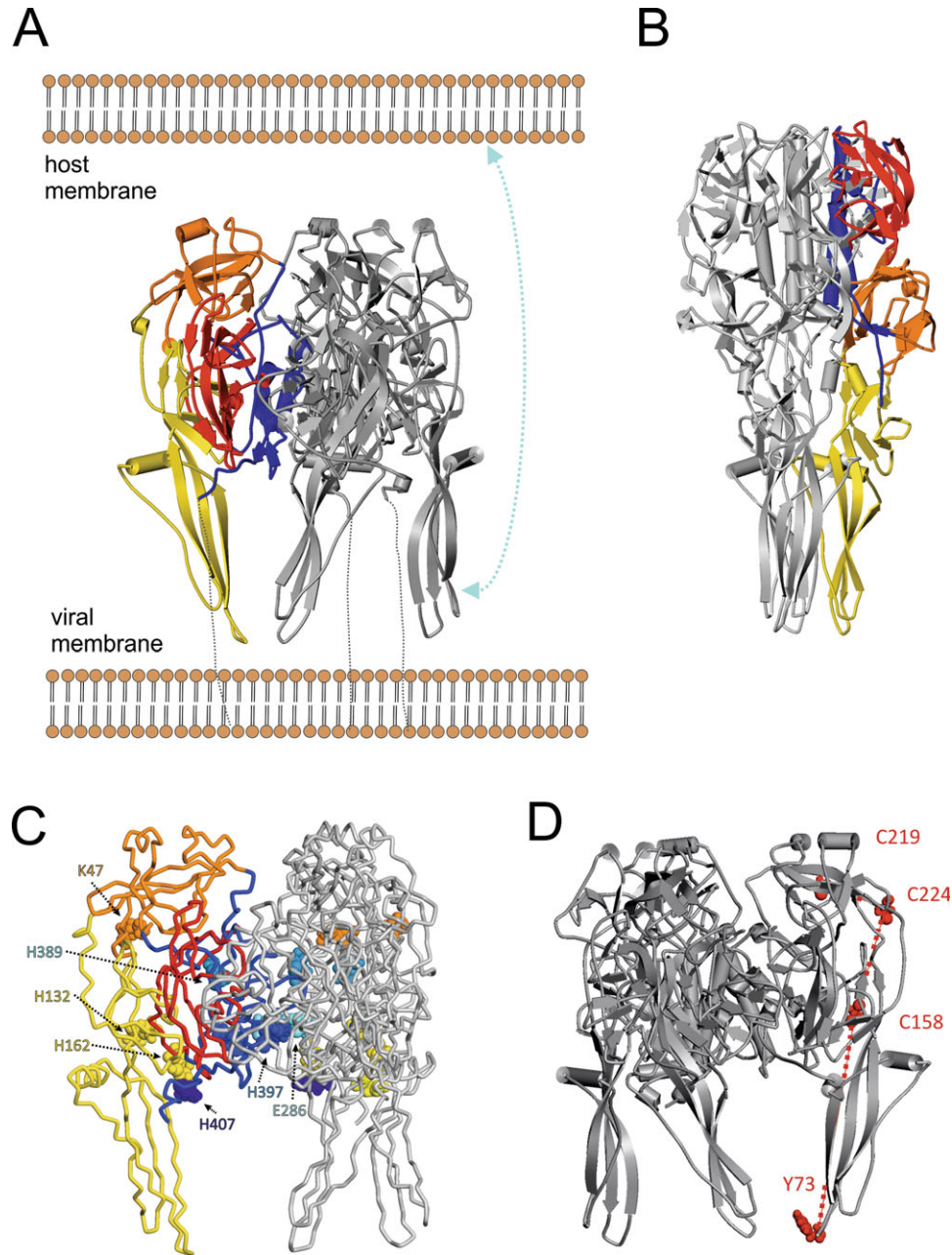
Figure 1

A: Trimer structure of the VSV-G prefusion conformation. Two monomers are colored gray, one monomer is shown in domain coloring (Domain I: red; Domain II: blue; Domain III: orange; Domain IV: yellow). Anchoring in the viral membrane is schematically depicted by gray dotted lines for the prefusion trimer. A cyan arrow indicates the motion of Domain IV containing the fusion loops toward the host cell membrane that occurs during the fusion process. **B**: Trimer structure of the VSV-G postfusion conformation (color coding as in Panel A; rotated 180° around the vertical axis with respect to Panel A. **C**: VSV-G prefusion trimer in tube representation (color coding as in Panel A). Differentially protonated residues are shown in space-filled representation. Residues are colored according to their domain location: K47 (Domain III) in orange; H132 and H162 (Domain IV) in yellow; E286 (Domain II) in cyan; H389, H397, and H407 (Domain II) in light blue, blue, and dark blue, respectively. **D**: Schematic representation showing the C219-C224-C158-Y73 dihedral angle. C219, C224, C158, and Y73 are shown in red; axes of dihedral angle between C_α atoms are indicated as dotted red lines.

clarified. With respect to the cascade of the rearrangement events, it is not yet known whether Domain IV reorientation represents the initial step of conformational change or whether elongation of the central domain II helices occurs first.[15] Previous investigations could not resolve the sequence of events, as they were solely based on steric considerations, instead of molecular mechanistic or dynamic analyses, and only focused on the monomer conformation.

To elucidate the molecular mechanisms of the initial steps of VSV-G rearrangement that lead to membrane fusion, we first calculated the protonation probability of the titratable groups in the VSV-G prefusion conformation. Subsequently, 50-ns all-atom molecular dynamics (MD) simulations of the VSV-G prefusion trimer were performed at two different protonation states, one corresponding to pH 7 (VSV-G7) and the other corresponding to pH 5 (VSV-G5). This study revealed a high mobility of Domain IV and also allowed the identification of the key residues that are differentially protonated between pH 5 and pH 7.

MATERIALS AND METHODS

The prefusion conformation (PDB: 2J6J) of VSV-G was simulated at two different protonation states. To this end, the protonation states of all titratable residues of VSV-G at pH 7 and pH 5 were determined using *in silico* titration assays (for the titration curves, refer to Supporting Information Fig. S1). The electrostatic potential was calculated using the Poisson-Boltzmann equation as implemented in the MEAD program suite.[16,17] The dielectric constant of the molecular interior was set to 4.0, and the ionic strength was set to $0.1M$. Default values were kept for all other parameters. The first two focusing steps of the calculation of the electrostatic potential were performed using a grid of 121^3 points with a grid spacing of 2.0 and 1.0 Å. For the final focusing step, a grid of 181^3 points with a grid spacing of 0.15 Å was used. The protonation probability curves were obtained by a Metropolis Monte Carlo algorithm.[18] For each pH step of 0.2 pH units, the calculation consisted of 100 equilibration scans and 10,000 production scans at 300 K. The resulting protonation states of differentially protonated titratable amino acids of VSV-G at pH 7 and pH 5 are listed in Supporting Information Table S1 and their position in the structure is shown in Figure 1(C). The side chains of all titratable amino acids were adjusted manually according to the results of the *in silico* titrations. For surface residues with differing protonation probabilities between pH 5 and pH 7, standard protonation states were adopted in both simulations.

All full-atom MD simulations presented in this work were performed using AMBER 9[19–21] with the parm99SB force field[22,23] and the TIP3P water model.[24] Simulations were performed in a periodic water box with at least 10 Å of solvent around every atom of the solute. An appropriate number of counter ions was added to neutralize the charges of the systems, and the Particle Mesh Ewald summation method[25] was used to calculate the long-range electrostatic interactions. All structures were minimized in a three-step procedure using the SANDER module of AMBER following a previously established protocol.[26–28] MD simulations were performed using the SHAKE procedure[29] to constrain all bonds involving hydrogen atoms. The integration time step of the simulation was 2 fs, and a 10 Å cutoff was used for the nonbonded interactions, which were updated every 15 steps. The temperature of each system was gradually heated to 310 K during the first 20 ps using a time step of 0.5 fs. Subsequently, 50-ns MD simulations were performed for data collection. An additional 50-ns simulation was performed for reduced VSV-G at 298 K (pH 5). This simulation was performed for control purposes and only analyzed with respect to the Domain IV mobility presented in Supporting Information Figure S7. Backbone root mean square deviation (RMSD) values were calculated based on the Cα, C, and N atoms of the respective residues. For the visualization, structural, and energetic analyses of the trajectory data, the programs DSSP,[30] Sybyl 7.3,[31] DS ViewerPro Suite 6,[32] and AMBER[21] were used.

Energetic analyses were performed on 900 snapshots taken between 5 and 50 ns of simulation with an interval of 50 ps. The Molecular Mechanics Generalized Born Surface Area (MM/GBSA) method implemented in AMBER10[33] was used to calculate the interaction energy E_{int} according to the standard equation for protein–ligand complexes:

$$\Delta E_{int} = E_{complex} - (E_{ligand} + E_{receptor}).$$

Each energy term represents the sum of the MM interaction energy (E_{MM}) and a solvation term (E_{sol}):

$$E = E_{MM} + E_{sol}.$$

The contribution of E_{MM}, which was calculated with the sander module of AMBER, represents the MM energy interaction between ligand and receptor and comprises electrostatic (ele) and van der Waals (vdw) energy terms.

The solvation energy E_{sol} takes into account the energy contribution of solvation effects. It combines terms for electrostatic and nonpolar energy. The electrostatic term was calculated using the Amber Generalized Born model 2[34] with standard settings. The nonpolar term (E^{np}) is defined as a function of the solvent-accessible surface area (SA)[35]:

$$E^{np} = \gamma \times SA + b,$$

with $\gamma = 0.00720$ kcal mol^{-1} Å^{-2} and $b = 0.00$ kcal mol^{-1}. To investigate the total energy difference of H132 and H407 between the prefusion conformation and four snapshots (5, 15, 30, and 50 ns) of the low-pH MD trajectory, we calculated the protonation probabilities for the snapshot structures, using the same MEAD setup as for the prefusion structure. The total energy difference is given by the following equation[36]:

$$\Delta E_{total} = \Delta E_{solv} + \Delta E_{rest} = RT \ln[(<x>_{pre}$$
$$(1-<x>_{snapshot}))((1-<x>_{pre})<x>_{snapshot})^{-1}].$$

Here, $<x>_{pre}$ and $<x>_{snapshot}$ indicate the protonation probability of the residue at pH 5 in the prefusion
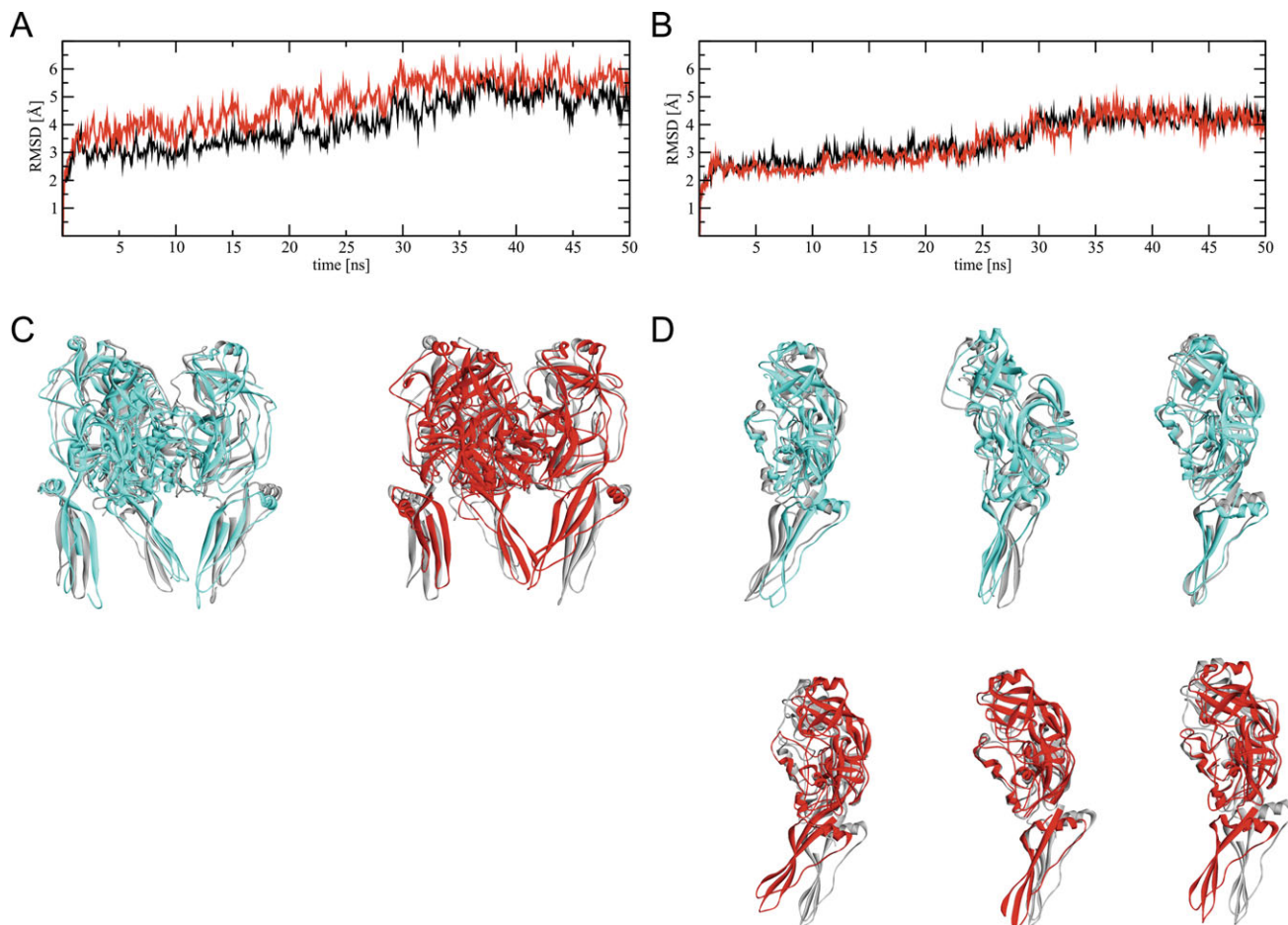
Figure 2
Total RMSD of trimeric VSV-G (**A**) and RMSD of VSV-G core without Domain IV (**B**). VSV-G7 is shown in black; VSV-G5 in red. Overlays of VSV-G trimers (**C**) and individual subunits (**D**) for the minimized structure (gray) with the representative structure of most frequently sampled hierarchical RMSD cluster (cyan for pH 7 simulation and red for pH 5 simulation).

structure and in the snapshot structure, respectively. The total energy change consists of a polar solvation term ΔE_{solv}, charge–charge interactions, and entropic contributions. The latter two contributions are combined in ΔE_{rest}. A Poisson-Boltzmann approach was used to determine ΔE_{solv} for H132 and H407. The same MEAD setup as in the titration assays was applied, except that all other titratable residues adopted the protonation state of the MD simulation at pH 5.

Coarse-grained MD simulations were performed using RedMD 2.0[37] with the HIV-1 protease force field combined with Coulomb interactions. Each amino acid was represented by one node, whose mass and charge correspond to the values of the full-atom model at pH 5. Default force-field parameters were used. After minimization and equilibration for 75 ns under Berendsen temperature control, a 300-ns simulation was performed in the microcanonical ensemble using a velocity Verlet integration algorithm with a time step of 0.02 ps. A temperature

of 310 K was applied. Translation of the center of mass and rotation around it were removed every 100 steps. Principal components were calculated by a self-written program and visualized in VMD[30] with the Normal Mode Wizard plugin of ProDy.

RESULTS AND DISCUSSION

Global dynamics of VSV-G investigated by full-atom and coarse-grained simulations

Based on the 50-ns trajectory data from the full-atom simulations, the global dynamics were analyzed to gain first insight into the general behavior of VSV-G in the two different protonation states. The RMSD analyses of the full trimer structure [Fig. 2(A)] and of the protein core (Domains I–III) without Domain IV [Fig. 2(B)] show that Domain IV significantly contributes to the overall RMSD, thus indicating a high mobility of this

domain. The high mobility of Domain IV with respect to the protein core can also be seen from the overlays of snapshots from the VSV-G7 and VSV-G5 simulations taken every 10 ns with the minimized structure (Supporting Information Fig. S2). Using hierarchical RMSD clustering, the most frequent conformations were identified from the VSV-G7 and VSV-G5 simulations [Fig. 2(C,D)]. The most prevalent cluster conformation at pH 7 is sampled in 20.2% of all snapshots, and the representative structure for this cluster shows an RMSD value of 3.71 Å to the initial structure. At pH 5, the most prevalent conformation has an occurrence of 28.2% with the representative cluster structure displaying a slightly higher total RMSD of 5.28 Å to the starting structure. In both simulations, the large RMSDs can mainly be attributed to motions of Domain IV, whereas the VSV-G core remains rather rigid.

The present simulations in explicit solvent were able to identify enhanced motions of Domain IV, whereas the remaining domains exhibited only small fluctuations. For large systems like VSV-G (1239 amino acids, more than 40,000 water molecules), such simulations are computationally expensive and are therefore limited on their time scale. Therefore, we also tested an alternative method (RedMD), which allows enhanced sampling of coarse-grained molecule models thus offering the possibility to detect larger-scale motions. The RedMD simulation confirms the high flexibility of Domain IV (Fig. 3), which is also reflected in the significant contribution of this domain to the overall RMSD of the system (Supporting Information Fig. S4). The fusion loops of Domain IV fluctuate around the position of the X-ray structure without preferring a certain direction. The dynamics of the simulation can be described as motion along principal components, with the modes with highest eigenvalues showing the largest displacements (Fig. 3 and Supporting Information Fig. S5). Thus, the fusion loops can move at low energetic cost both in the full-atom and in the coarse-grained model, because they are only subjected to few constraints.

From previous studies, it was not clear whether the motion of Domain IV represents the initial step of pH-induced membrane fusion or whether other conformational changes have to occur first. In particular, it has been suggested that an elongation of the central domain II helices has to occur first.[15] For that reason, we have also inspected the secondary structure, especially N-terminal of the α-helical region (residues 273–290) of Domain II in the context of potential helix elongation. Analysis of the simulation in explicit solvent revealed no significant differences of this helical region between VSV-G7 and VSV-G5 (Supporting Information Fig. S3). The coarse-grained simulation also revealed no significant structural rearrangements for the protein core, and the length of the secondary structure elements in Domain II remains rather constant. The C_α atoms of T265 and
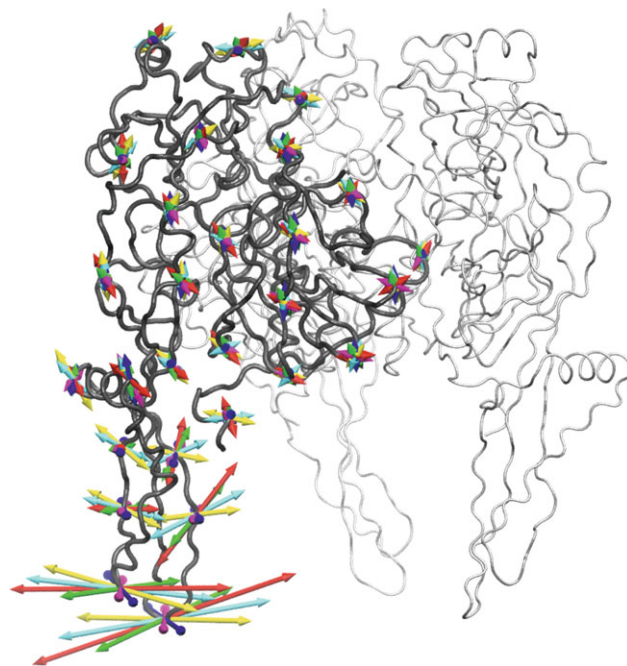

Figure 3

Structure of VSV-G indicating the direction of the six principal modes with the highest eigenvalues (vector presentation) deduced from the coarse-grained RedMD simulation. For clarity of presentation, eigenvectors are only shown for representative residues of the individual domains of Subunit A. (Refer to Supporting Information Fig. S5 for an explicit presentation of the eigenvectors for all residues.) The arrow lengths are proportional to the standard deviation along the mode of the corresponding residue.

R292 have a distance of 41 Å in the postfusion conformation, where they mark the termini of the elongated α-helix. In the RedMD simulation, this distance fluctuates continuously around a value of 24 Å, which corresponds to the distance in the X-ray structure of the prefusion conformation [Supporting Information Fig. S4(B)].

In summary, both simulation methods suggest that Domain IV motions represent an initial step in VSV-G membrane fusion, whereas changes on the level of secondary structure, which were postulated from the comparison with the postfusion form,[15] are expected to occur at a later time point. The fact that the RedMD does not reveal large-scale rearrangement when compared with the simulation in explicit solvent suggests that these remaining structural changes during pH-induced membrane fusion occur on time scale not yet accessible to simulation techniques or might require the presence of the host membrane.

Differentially protonated residues of the domain IV interface with the protein core

The simulations above demonstrated that Domain IV exhibits the highest mobility rendering it a likely candi-

date for the initial motions in pH-driven rearrangement. We therefore analyzed the interface of Domain IV with the protein core to verify whether this interface becomes differentially protonated. Domain IV has two major interfaces with the protein core. One lies between the proximal part of Domain IV and Domain I and the other involves the more distal part of Domain IV and the very C-terminal portion of a loop extending from Domain II [Fig. 1(A,C)]. This C-terminal stretch continues toward the transmembrane portion of VSV-G, which is not resolved in the crystal structure and was therefore omitted from the simulations. In each of these two interfaces, there exists one pair of structurally neighboring highly conserved amino acids that is affected by differential protonation (for a sequence alignment, refer to Supporting Information Fig. S6).

The first pair, H132–K15, is located in the Domain IV–Domain I interface [Fig. 4(A)]. H132 is ϵ-protonated at pH 7 and additionally δ-protonated at pH 5. H132 is strictly conserved (Supporting Information Fig. S6), and for K15, only one conservative exchange to an arginine is recorded for Piry virus, suggesting that the interaction between differentially protonated H132 and a basic residue in sequence position 15 is functionally important. Analysis of the interatomic distance between the two closest side-chain atoms in the crystal structure (H132-$N_{\epsilon 2}$ and K15-N_{ζ}) shows that this distance increases in VSV-G5 [Fig. 4(B), upper panel, red curve] from 4.5 Å up to 9 Å over time and exhibits large fluctuations in the second half of the simulation. In contrast, in VSV-G7 [Fig. 4(B), upper panel, black curve], the contacts between both side chains are preserved over the entire simulation. Major differences between pH 5 and pH 7 are also observed in the distance between H132-C_{α} and K15-C_{α} [Fig. 4(B), lower panel]. This indicates that the side-chain motion detected at pH 5 also causes a displacement of the protein backbone, whereas such an effect is not observed at pH 7.
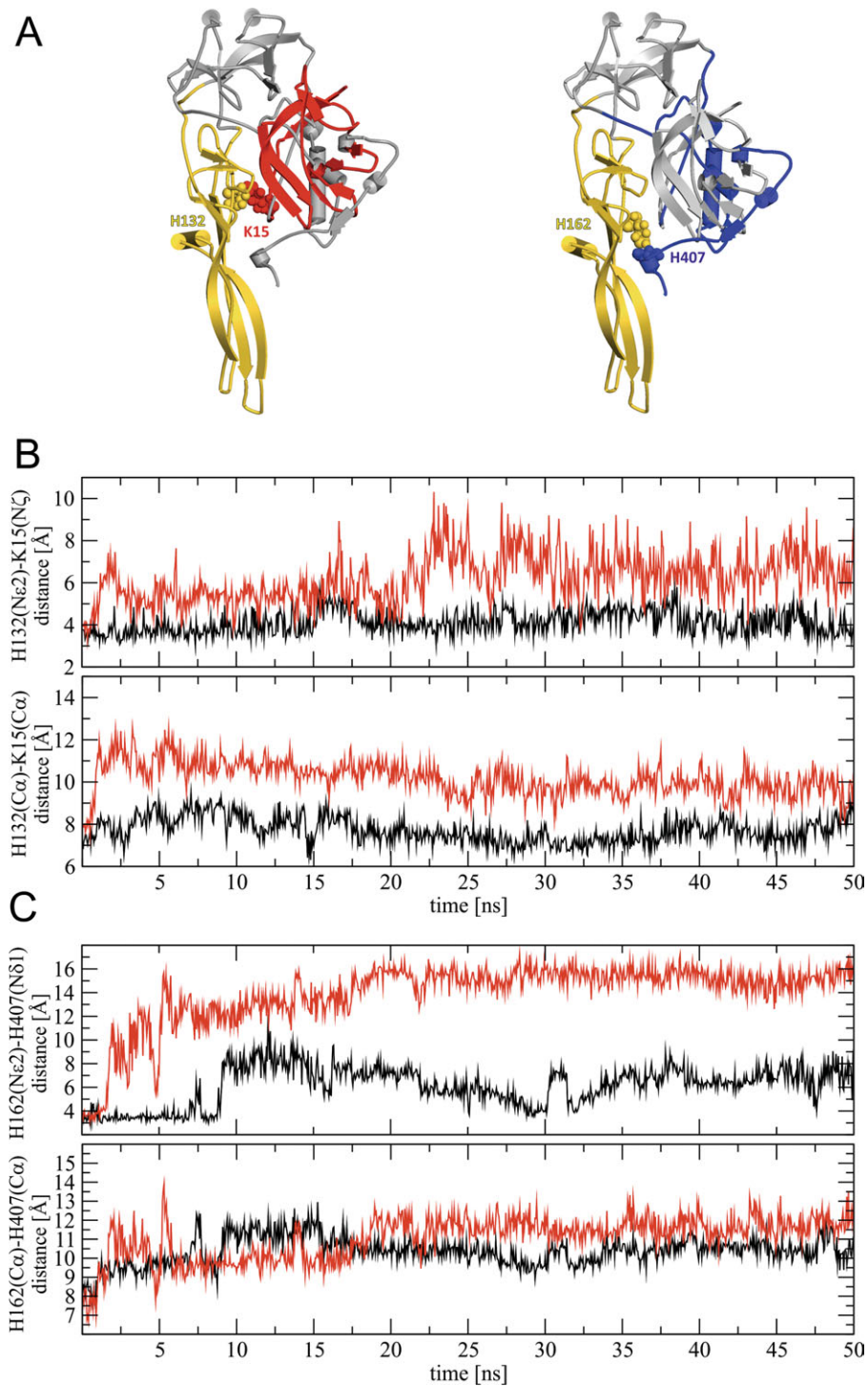
These local rearrangements of side chains and backbone at pH 5 are also clearly seen in a structure overlay of VSV-G5 after minimization and after 5.1 ns of simulation [Fig. 5(A)]. This structural view shows that the side chain of K15 has rotated away from the side chain of H132 when compared with the minimized structure. The backbones of Domain IV and Domain I have also moved apart. Similar effects have been well studied and described as a mechanism for the induction of viral membrane fusion by pH-sensitive histidine switches.[8,38] Moreover, H132 protonation has been experimentally shown to be crucial for VSV-G fusion capacity.[14] Therefore, the findings of the current study are in line with other experimental and theoretical work on the subject.

The second pair, H162–H407, is located in the Domain IV–Domain II interface [Fig. 4(A)]. These residues have previously been suggested to be involved in a molecular swi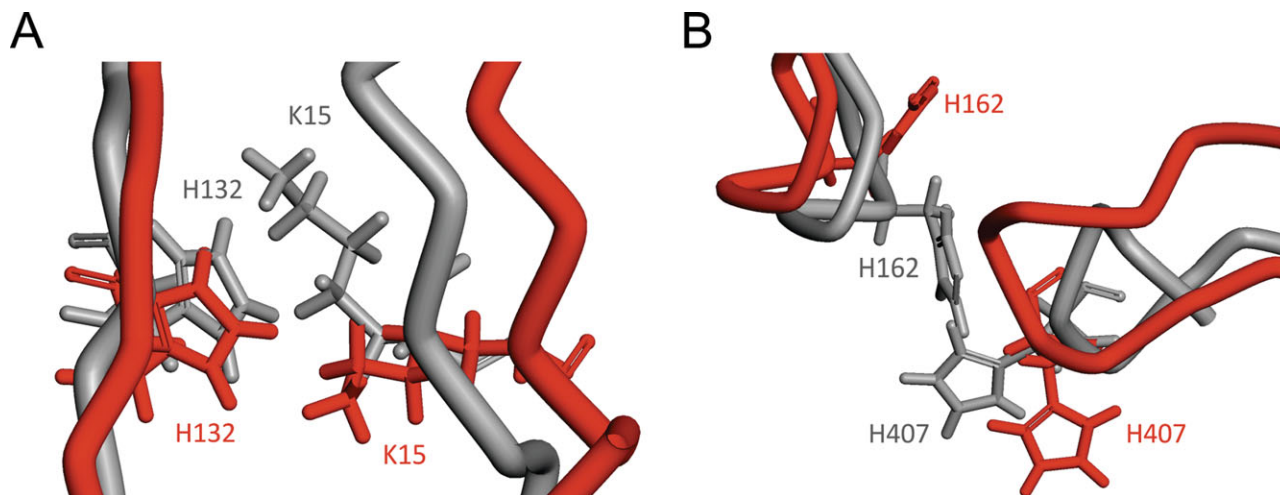tch based on their location in the prefusion structure.[13,15] The current study reveals that H162 is single protonated at both pH states. However, it is ϵ-protonated at pH 7 and δ-protonated at pH 5. H407 is ϵ-protonated at pH 7 and additionally δ-protonated at pH 5. Both histidines are fully conserved in the rhabdovirus family (Supporting Information Fig. S6), stressing the potential importance of their pH-sensitive interaction. Analysis of the interatomic distance between the side-chain atoms closest to each other in the crystal structure (H162-$C_{\epsilon 1}$ and H407-$N_{\epsilon 2}$) reveals that at pH 5, the side chains continuously drift apart in the first half of the simulation [Fig. 4(C), upper panel] reaching a plateau value of ~ 16 Å after 20 ns. When compared with VSV-G5, the side-chain distance changes observed for the H162–H407 interaction are much smaller in VSV-G7 [Fig. 4(C), upper panel]. This effect is further illustrated in Figure 5(B), where an overlay of the minimized VSV-G5 structure (gray) and a snapshot after 5.1 ns (red) is shown. Here, both side chains are completely rotated away from each other, disrupting all side-chain interactions. The significance of the C-terminal loop as a trigger for membrane fusion is in line with previous experimental studies revealing that mutations in the respective loop abolish fusion.[39,40]

The drifting apart of the residue pairs H132–K15 and H162–H407 due to differential protonation is an electrostatic effect, which is caused by unfavorable charge–charge interactions and by burial of charges inside the protein. To quantify this effect, a Poisson-Boltzmann approach was used to calculate the total energies and the solvation energies of the differentially protonated residues H132 and H407 for the prefusion structure and for four snapshot conformations of the low-pH MD simulation. In the case of the H132–K15 pair, the conformational changes mainly compensate for the repulsion between the two positively charged residues. In contrast, the driving force behind the growing distance between H407 and H162 is the increasing solvation of H407, which leads to solvation energy gains up to 1.7 kcal mol^{-1} (Table I). The total energy change is usually smaller than its single contributions, because the effects of charge–charge interactions and entropy are often contrary to the solvation effect. For these residues, we have additionally verified that the initially chosen protonation states are still valid at the end of the low-pH MD simulation (see Supporting Information Fig. S8). The results show that the titration curves for H407 and H132 are shifted to higher pH values, showing that double protonated H407 and H132 are a reasonable choice for the low-pH simulations. The double protonation is more stabilized in the relaxed structure after 50 ns of MD simulation when compared with the initial structure.

The identification of two differentially charged histidines at the interface between Domain IV and the protein core also offers support for a recent study that questioned the previous hypothesis of a single histidine

Figure 4

A: Schematic representation of VSV-G Subunit A showing the two conserved interacting pairs H132–K15 (left) and H162–H407 (right). Domain IV (residues 50–180) is colored yellow; Domain I (residues 1–17 and 310–383) and Domain II (residues 18–35, 259–310, and 384–413) are colored red and blue, respectively. Other residues are shown in gray. **B**: Interatomic distances between H132-$N_{\epsilon 2}$ and K15-N_{ζ} (upper panel) and H132-C_{α} and K15-C_{α} (lower panel). VSV-G7 is shown in black; VSV-G5 is shown in red. **C**: Interatomic distances between H162-$N_{\epsilon 2}$ and H407-$N_{\delta 1}$ (upper panel) and H162-C_{α} and H407-C_{α} [lower panel; color coding as in (B)].

Figure 5
Overlays of VSV-G at pH 5 after minimization (gray) and after 5.1 ns of simulation (red). **A:** Zoom on Subunit A, residues H132 and K15. **B:** Zoom on Subunit A, residues H162 and H407. Other residues are omitted for clarity.

switch being sufficient to induce conformational changes in a large system such as a viral fusion protein.[41] A co-operative function of H132–K15 and H162–H407 in the "unlocking" of Domain IV therefore appears highly plausible. We do not find any evidence for the role of H60 as a pH-induced trigger, as it was postulated previously.[13,15] The present *in silico* titration experiments indicate that H60 is not differentially protonated between VSV-G7 and VSV-G5 (Supporting Information Fig. S1), rendering its role for a pH-induced conformational change less likely.

Table I
Total Energy Difference ΔE_{tot}, Solvation Energy Difference ΔE_{solv}, and Rest of the Total Energy Difference ΔE_{rest} of H132 and H407 Between the Prefusion Structure and Snapshots from the Low-pH MD Simulation for Each Subunit

	Subunit A			Subunit B			Subunit C		
	ΔE_{tot}	ΔE_{solv}	ΔE_{rest}	ΔE_{tot}	ΔE_{solv}	ΔE_{rest}	ΔE_{tot}	ΔE_{solv}	ΔE_{rest}
H132									
5	−1.58	0.46	−2.04	0.22	−0.30	0.52	−2.57	0.16	−2.73
15	—	0.54	—	−0.54	−0.63	0.09	1.47	0.09	−1.56
30	0.87	−1.07	1.94	−0.33	−0.59	0.26	4.56	−0.55	5.11
50	−0.25	−1.35	1.10	0.03	−0.57	0.60	−1.58	−0.62	−0.96
H407									
5	−0.74	−0.76	0.02	−1.63	0.78	−2.41	−1.04	−1.09	0.05
15	−0.20	−0.71	0.51	−1.08	−1.26	0.18	−0.41	−1.66	1.25
30	−1.37	−1.52	0.15	−0.86	−1.52	0.66	−0.63	−1.28	0.65
50	−0.37	−0.46	0.09	−0.63	−1.48	0.85	−0.49	−0.06	−0.43

ΔE_{tot} was calculated as described in the Materials and Methods section. Negative total energy differences show that the double protonation is stabilized in the snapshot structure when compared with the prefusion structure. H132 is fully protonated at pH 5 after 15 ns of MD simulation. Therefore, ΔE_{tot} of H132 cannot be determined for this structure by the described method. The solvation energies were calculated by a Poisson-Boltzmann approach. Negative values indicate a better solvation in the snapshot conformation. ΔE_{rest} accounts for charge–charge interactions and entropic contributions. All values are expressed in kcal mol^{-1}.

Characterization of the domain IV–core interface

To investigate the consequences of differential histidine protonation on the Domain IV interaction with the protein core, energetic analyses of the respective interface were performed. Calculation of the mean interaction energy of Domain IV with the protein core (Domains I–III) over simulation (5–50 ns) provided further insight (Table II). For all three subunits, the interaction of Domain IV with the protein core is weakened on protonation by 2.4–26.2 kcal mol^{-1}.

In addition, we investigated the correlation between interaction energy and the orientation of Domain IV with respect to the protein core. For that purpose, the dihedral angle between the C_α atoms of C219, C224, C158, and Y73 was chosen as a measure for Domain IV conformation [Fig. 1(D)]. The cysteine residues 219, 224, and 158 are located in the core of VSV-G and are stabilized by disulfide bonds locking their positions. With these fixed reference points, the fourth residue tyrosine 73, located at the tip of the longer Domain IV β-strand, serves to monitor the Domain IV motions with respect to the protein core (Domains I–III). Similar geometric criteria have been already used in previous investigations to study domain–hinge motions.[42,43]

The Domain IV interaction energy (E_{int}) with the protein core is plotted against the dihedral angle of the C_α atoms of C219, C224, C158, and Y73. At pH 7 [Fig. 6(A), black dots], all three subunits show rather symmetrical angle distributions with the most favorable energies in Subunit A followed by Subunit B. The energy plots in Figure 6(A) also reveal that the interaction at pH 5 (red dots) is weaker than at pH 7 (black dots) for most of the dihedral angles sampled. This observation indicates that

Table II
Interaction Energies E_{int} Between VSV-G Domain IV (Residues 51–180) and the Protein Core (Residues 1–47 and 184–413) at pH 5 and pH 7 for Each Subunit
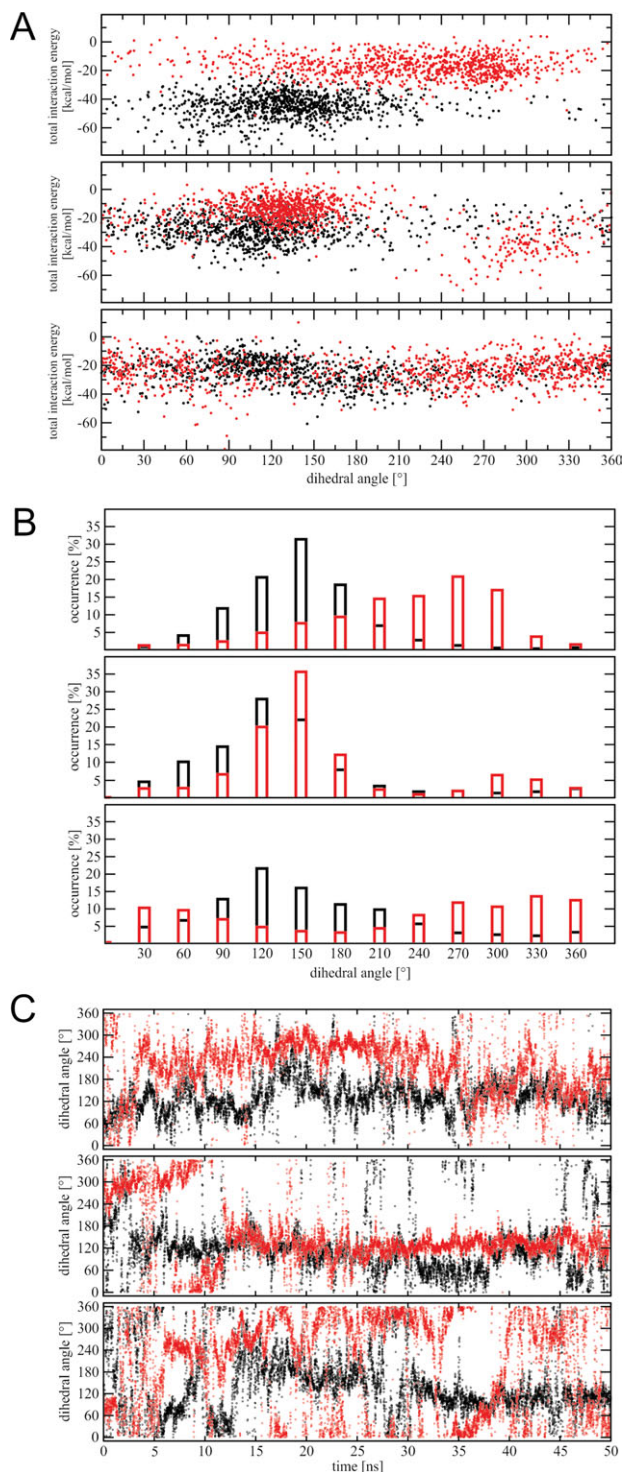
	Subunit A	Subunit B	Subunit C
E_{int} (Domain IV) pH 7	−43.54 (±0.27)	−27.73 (±0.29)	−24.42 (±0.30)
E_{int} (Domain IV) pH 5	−17.33 (±0.25)	−15.35 (±0.32)	−22.03 (±0.29)
ΔE_{int}	26.21 (±0.37)	12.38 (±0.43)	2.39 (±0.41)

ΔE_{int} gives the difference of the interaction energies measured at pH 5 and pH 7. All values are expressed in kcal mol^{-1}. The standard error is given in parentheses.

the core–Domain IV interaction is generally destabilized at low pH. At pH 5, there is also a considerable variation between the subunits regarding both dihedral and energy distribution [Fig. 6(A), red dots]. In Subunit A, the interaction is weakened by low pH when compared with pH 7, regardless of the dihedral conformation Domain IV adopts. Yet, larger dihedral values between 240° and 270° are more frequently sampled [Fig. 6(A), upper panel]. In VSV-G5, Subunit B dihedral distribution largely follows that of VSV-G7, although at a higher energy level. Larger angles between 240° and 330° are energetically favorable, but are only occasionally sampled [Fig. 6(A), middle panel]. At pH 7, these larger angles are also infrequently sampled, but are not energetically beneficial. Subunit C displays a wider dihedral distribution at pH 5; however, no significant energetically differences were observed between pH 5 and pH 7 [Fig. 6(A), lower panel].

Although it appears that pH 5 affects the sampling of Domain IV to a certain degree, there is no clear correlation between the energy of a conformation and the frequency of its sampling. In addition, the sampling of the individual subunits at pH 5 is rather different, which can be seen from a histogram plot of the dihedral angles [Fig. 6(B)]. The latter effect is also observed in a control simulation performed at pH 5 (298 K; Supporting Information Fig. S7). In contrast, in the RedMD simulation at pH 5, the Domain IV of all subunits fluctuates around the torsion angle of 156° present in the prefusion crystal structure.

This apparent difference between the full-atom and coarse-grained simulations might have the following explanations. The full-atom simulation of 50 ns is probably too short to allow an exhaustive sampling of all the Domain IV orientations with respect to the protein core. Evidence for this finding comes from the different sampling of the individual domains and from the observation that there are only few transitions between the individual domain orientations [Fig. 6(C) and Supporting Information Fig. S7(B)]. The fact that no differences in the sampling of Domain IV are detected in the coarse-grained simulation might result from the more comprehensive sampling of this method when compared with

Figure 6
A: Plot of the interaction energy between Domain IV and protein core versus the dihedral angle between C_α atoms of C219, C224, C158, and Y73 for each subunit: Subunit A (upper panel), Subunit B (middle panel), and Subunit C (lower panel). **B**: Histograms showing the distribution of the dihedral angle between C_α atoms of C219, C224, C158, and Y73 for each subunit: VSV-G7 is shown in black; VSV-G5 is shown in red. **C**: Plot of the C219-C224-C158-Y73 dihedral angle as a function of the simulation time for each of the subunits.

Table III
Interaction Energies E_{int} Between One Individual Subunit and the Two Remaining VSV-G Subunits at pH 5 and pH 7

	Subunit A with BC core	Subunit B with AC core	Subunit C with AB core
E_{int} (subunit) pH 7	−93.30 (±0.35)	−103.63 (±0.32)	−91.86 (±0.32)
E_{int} (subunit) pH 5	−108.93 (±0.36)	−118.53 (±0.39)	−114.66 (±0.34)
ΔE_{int}	−15.63 (±0.50)	−14.90 (±0.51)	−22.80 (±0.47)

ΔE_{int} gives the difference of the interaction energies measured at pH 5 and pH 7. All values are expressed in kcal mol^{-1}. The standard error is given in parentheses.

Table IV
Interaction Energies E_{int} Between the C-Terminal Loop (387–400) and the Adjacent VSV-G Subunit at pH 5 and pH 7

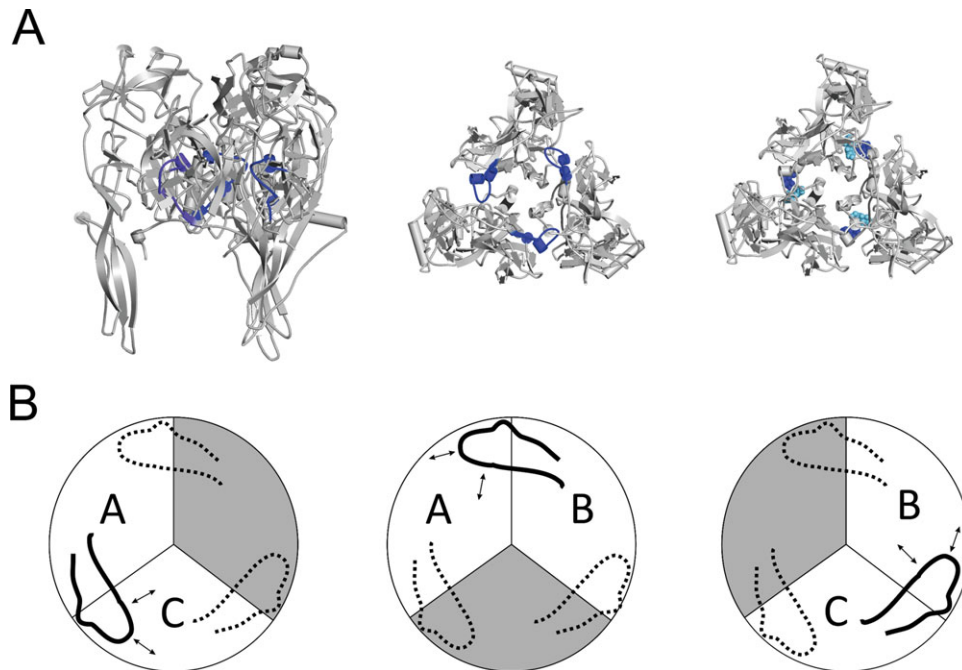|	Loop A–Subunit C	Loop B–Subunit A	Loop C–Subunit B
E_{int} (loop) pH 7	−16.51 (±0.34)	−16.05 (±0.23)	−27.90 (±0.19)
E_{int} (loop) pH 5	−31.42 (±0.23)	−34.54 (±0.24)	−39.13 (±0.24)
ΔE_{int}	−14.91 (±0.41)	−18.49 (±0.33)	−11.23 (±0.30)

ΔE_{int} gives the difference of the interaction energies measured at pH 5 and pH 7. All values are expressed in kcal mol^{-1}. The standard error is given in parentheses.

the full-atomistic simulation. However, one should also keep in mind that the coarse-grained method may miss certain effects relevant for Domain IV dynamics, for example, due to the lack of a solvation model. Solvation was shown above to represent an important force for driving structural changes in the vicinity of the differentially protonated histidines in the Domain IV–core interface (Table I).

In summary, the present simulations do not allow a final conclusion, whether the differential protonation of the histidines in the Domain IV–core interface also induces an altered sampling of Domain IV at pH 5. The latter effect would be expected in the light of the large-scale structural changes that occur during membrane fusion; however, the majority of these changes probably occur on times scales that are computationally not yet accessible.

Stability of the VSV-G trimer

Previous investigators also speculated whether the large-scale rearrangements that have to occur during membrane fusion might be possible for the intact trimer or whether the VSV-G trimer temporarily dissociates during conformational rearrangement.[13,15]

As an ongoing dissociation should be reflected in a weaker interaction energy of the subunits, energetic analyses of VSV-G5 and VSV-G7 were performed. Unexpectedly, this analysis reveals that each of the subunits interacts stronger with the remaining subunits at pH 5

Figure 7
A: Schematic structural representation of the VSV-G trimer structure as side view (left) and top view (middle). The C-terminal loops (residues 387–400) extending from Domain II are highlighted in blue. In the top view on the right, residues H22 (light blue) and H397 (blue) are shown in space-filled representation. **B:** Schematic drawing of the trimer (top view) with C-terminal loops (represented as bold and dotted black lines) to illustrate energetic analyses in Table IV.
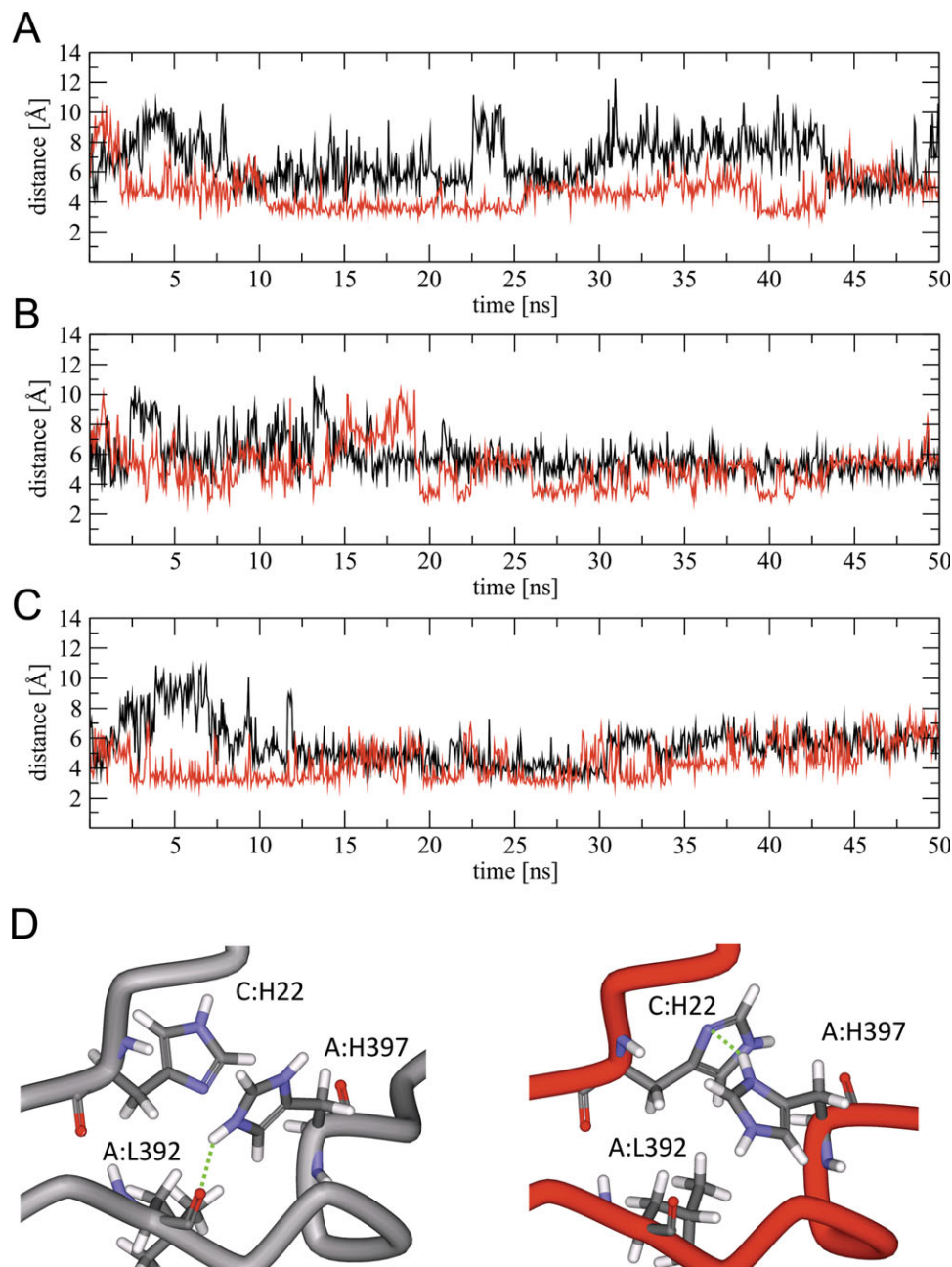
Figure 8

A–C: Interatomic intersubunit distances between the side-chain atoms H397-$N_{\delta1}$ and H22-$N_{\delta1}$ (lower panels) at pH 7 (black) and pH 5 (red) over the course of simulation. Distance between A: H397 and C: H22 (A), distance between B: H397 and A: H22 (B), and distance between C: H397 and B: H22 (C). **D:** VSV-G at pH 5 after minimization left (gray), and after 15 ns of simulation right (red). Zoom on Subunit A–C interface, residues H397, L392, and H22 are shown as sticks and labeled according to their subunit. Other residues are omitted for clarity. Hydrogen bonds are depicted as dotted green lines.

when compared with pH 7 (Table III). The differences between both pH values are in the range from −14.9 to −22.8 kcal mol^{-1} depending on the subunit investigated.

A closer analysis revealed that the stronger interaction energy at pH 5 (shown in Table III) can almost exclusively be attributed to one single loop (residues 387–400) extending from Domain II and interacting with the adja-cent subunit's N-terminus and core [Fig. 7(A)]. More precisely, the C-terminal loop of Subunit A interacts with the N-terminus and core of Subunit C; the loop of Subunit B interacts with Subunit A; and the Subunit C loop interacts with Subunit B [Fig. 7(B)]. At pH 5, the inter-action of this loop with the adjacent subunit is increased by 11.2 to 18.5 kcal mol^{-1} (Table IV), thus representing

the main driving force behind the strengthening of the trimer interfaces.

A detailed inspection of amino acids in this loop and their structural location reveals another pair of histidines affected by differential protonation whose side chains are facing each other in the crystal structure: H397 and H22. H22 is ϵ-protonated at both pH states; H397 is ϵ-protonated at pH 7 and additionally δ-protonated at pH 5. H397 is not as strictly conserved as K15, H132, H162, and H407; however, fusion competence of VSV and rabies virus has been shown to be impaired by mutation in its close vicinity.[39,40,44]

Calculation of the intersubunit distances between H397-$N_{\delta 1}$ and H22-$N_{\delta 1}$ [Fig. 8(A–C)] reveals the formation of a close contact in VSV-G5 (red curves) that is not present in the crystal structure and is not formed at pH 7 (black curves). This tight polar interaction in VSV-G5 is rather stable in the interface between Subunits A and C [Fig. 8(A)], whereas larger fluctuations are observed in the two other interfaces [Fig. 8(B,C)]. Despite these larger fluctuations, distances of <4 Å are only observed in VSV-G5 but not for VSV-G7, indicating that the strength of the interaction correlates with the pH.

A structural view of side-chain rearrangement of H397 and H22 and the formation of a hydrogen bond between H397-$N_{\delta 1}$ and H22-$N_{\delta 1}$ is shown in Figure 8(D) for the interface between Subunits A and C. Although H397-$N_{\epsilon 1}$ forms an intrasubunit hydrogen bond with the carbonyl oxygen of L392 in the starting structure [Fig. 8(D), left], this bond is replaced by a new intersubunit interaction with H22 that is enabled by the presence of a proton to H397-$N_{\delta 1}$ under pH 5 conditions [Fig. 8(D), right].

In summary, all analyses show a strengthened interaction between the individual subunits at pH 5, rendering trimer dissociation at least in the initial stages of the fusion process highly unlikely. Residue 397, a differentially protonated histidine, contributes to the improvement of intersubunit adhesion by forming new contacts on protonation. The region of increased intersubunit stability is structurally very close to the Domains II–IV interface, where intrasubunit interactions are weakened between H162 and H407. This finding suggests that this strengthened intersubunit interaction at pH 5 might play a functional role in the initial step of conformation change by creating a rigid scaffold in the core that facilitates Domain IV rearrangement during membrane fusion.

CONCLUSIONS

In this study, the dynamics of the VSV-G protein was investigated at two representative protonation states corresponding to pH 7 and pH 5, respectively. Because of the size of the system (1239 amino acids, more than 40,000 water molecules) and the large number of differentially protonated residues, a comprehensive investigation of alternative protonation schemes by different simulations is computationally extremely demanding. Therefore, our simulations focused on a representative protonation state that is based on the protonation probabilities calculated for the VSV-G crystal structure by a Poisson-Boltzmann approach.

Two of the differentially protonated histidines identified by the respective approach (H132 and H407) represent promising triggers for pH-induced structural changes in VSV-G. They exhibit a pronounced position at functionally important[39,40,44] domain interfaces (Figs. 4 and 5), they are conserved in homologs (Supporting Information Fig. S6), and changes of their protonation state offer a structural explanation of the experimentally observed Domain IV rearrangement.[15] The energetic analysis revealed that in addition to electrostatic repulsion, the gain in solvation energy for the protonated histidines represents a further driving force for the structural changes and weakened interactions observed in the Domain IV–core interface. The results of this study thus enhance the mechanistic understanding of the initial steps of pH-dependent conformational changes in VSV-G and provide the basis for mutational studies, which will allow a further experimental dissection of the role of individual residues in the fusion process.

The dynamics of VSV-G was primarily studied using full-atomistic MD simulations in explicit solvent. In particular for large systems like VSV-G, this method is limited with respect to the time scales that can be investigated. Therefore, we additionally performed coarse-grained RedMD simulations. Both simulation methods consistently indicate that motions of Domain IV, which also contains the fusion loops, represent an initial step in VSV-G membrane fusion. The fact that the RedMD does not reveal large-scale rearrangement when compared with the simulation in explicit solvent suggests that these remaining structural changes during pH-induced membrane fusion occur on a time scale not yet accessible to simulation techniques.

REFERENCES

1. Helenius A, Kartenbeck J, Simons K, Fries E. On the entry of Semliki forest virus into BHK-21 cells. J Cell Biol 1980;84:404–420.
2. White J, Helenius A. pH-dependent fusion between the Semliki forest virus membrane and liposomes. Proc Natl Acad Sci USA 1980;77:3273–3277.
3. Harrison SC. Viral membrane fusion. Nat Struct Mol Biol 2008;15:690–698.
4. Kamman RL, Go KG, Muskiet FA, Stomp GP, Van Dijk P, Berendsen HJ. Proton spin relaxation studies of fatty tissue and cerebral white matter. Magn Reson Imaging 1984;2:211–220.

5. Backovic M, Jardetzky TS. Class III viral membrane fusion proteins. Curr Opin Struct Biol 2009;19:189–196.

6. Da Poian AT, Carneiro FA, Stauffer F. Viral membrane fusion: is glycoprotein G of rhabdoviruses a representative of a new class of viral fusion proteins? Braz J Med Biol Res 2005;38:813–823.

7. Harrison SC. The pH sensor for flavivirus membrane fusion. J Cell Biol 2008;183:177–179.

8. Kampmann T, Mueller DS, Mark AE, Young PR, Kobe B. The role of histidine residues in low-pH-mediated viral membrane fusion. Structure 2006;14:1481–1487.

9. Maeda T, Ohnishi S. Activation of influenza virus by acidic media causes hemolysis and fusion of erythrocytes. FEBS Lett 1980;122: 283–287.

10. Roche S, Gaudin Y. Characterization of the equilibrium between the native and fusion-inactive conformation of rabies virus glycoprotein indicates that the fusion complex is made of several trimers. Virology 2002;297:128–135.

11. Skehel JJ, Bayley PM, Brown EB, Martin SR, Waterfield MD, White JM, Wilson IA, Wiley DC. Changes in the conformation of influenza virus hemagglutinin at the pH optimum of virus-mediated membrane fusion. Proc Natl Acad Sci USA 1982;79:968–972.

12. Roche S, Bressanelli S, Rey FA, Gaudin Y. Crystal structure of the low-pH form of the vesicular stomatitis virus glycoprotein G. Science 2006;313:187–191.

13. Roche S, Rey FA, Gaudin Y, Bressanelli S. Structure of the prefusion form of the vesicular stomatitis virus glycoprotein G. Science 2007;315:843–848.

14. Carneiro FA, Stauffer F, Lima CS, Juliano MA, Juliano L, Da Poian AT. Membrane fusion induced by vesicular stomatitis virus depends on histidine protonation. J Biol Chem 2003;278:13789–13794.

15. Roche S, Albertini AA, Lepault J, Bressanelli S, Gaudin Y. Structures of vesicular stomatitis virus glycoprotein: membrane fusion revisited. Cell Mol Life Sci 2008;65:1716–1728.

16. Bashford D. An object-oriented programming suite for electrostatic effects in biological molecules: an experience report on the MEAD project Scientific Computing in Object-Oriented Parallel Environments. In: Scientific computing in object-oriented parallel environments. Ishikawa Y, Oldehoeft R, Reynders J, Tholburn M, editors. Vol. 1343. Berlin: Springer; 1997. pp 233–240.

17. Bashford D, Gerwert K. Electrostatic calculations of the pKa values of ionizable groups in bacteriorhodopsin. J Mol Biol 1992;224:473–486.

18. Ullmann GM, Knapp EW. Electrostatic models for computing protonation and redox equilibria in proteins. Eur Biophys J 1999;28: 533–551.

19. Case DA, Cheatham T, Darden T, Gohlke H, Luo R, Merz KM, Onufriev A, Simmerling C, Wang B, Woods R. The Amber biomolecular simulation programs. J Comput Chem 2005;26:1668–1688.

20. Case DA, Darden TA, Cheatham TE, III, Simmerling CL, Wang J, Duke RE, Luo R, Merz KM, Pearlman DA, Crowley M, Walker RC, Zhang W, Wang B, Hayik S, Roitberg A, Seabra G, Wong KF, Paesani F, Wu X, Brozell S, Tsui V, Gohlke H, Yang L, Tan C, Mongan J, Hornak V, Cui G, Beroza P, Mathews DH, Schafmeister C, Ross WS, Kollman PA. AMBER 9. San Francisco, CA: University of California; 2006.

21. Pearlman DA, Case DA, Caldwell JW, Ross WS, Cheatham TE, III, DeBolt S, Ferguson D, Seibel G, Kollman P. AMBER, a package of computer programs for applying molecular mechanics, normal mode analysis, molecular dynamics and free energy calculations to simulate the structural and energetic properties of molecules. Comput Phys Commun 1995;91:1–41.

22. Cheatham TE, III, Cieplak P, Kollman PA. A modified version of the Cornell et al. force field with improved sugar pucker phases and helical repeat. J Biomol Struct Dyn 1999;16:845–862.

23. Cornell WD, Cieplak P, Bayly CI, Gould IR, Merz KMJ, Ferguson DM, Spellmeyer DC, Fox T, Caldwell JW, Kollman PA. A second

24. generation force field for the simulation of proteins, nucleic acids and organic molecules. J Am Chem Soc 1995;117:5179–5197.

24. Jorgensen WL, Chandrasekhar J, Madura JD, Impey RW, Klein ML. Comparison of simple potential functions for simulating liquid water. J Chem Phys 1983;79:926–935.

25. Darden TA, York DM, Pedersen LG. Particle mesh Ewald. An N.log(N) method for Ewald sums in large systems. J Chem Phys 1993;98:10089–10092.

26. Dirauf P, Meiselbach H, Sticht H. Effects of the V82A and I54V mutations on the dynamics and ligand binding properties of HIV-1 protease. J Mol Model 2010;16:1577–1583.

27. Meiselbach H, Horn AH, Harrer T, Sticht H. Insights into amprenavir resistance in E35D HIV-1 protease mutation from molecular dynamics and binding free-energy calculations. J Mol Model 2007;13:297–304.

28. Wartha F, Horn AHC, Meiselbach H, Sticht H. Molecular dynamics simulations of HIV-1 protease suggest different mechanisms contributing to drug resistance. J Chem Theory Comput 2005;1:315–324.

29. Ryckaert JP, Ciccotti G, Berendsen HJC. Numerical integration of the Cartesian equations of motion of a system with constraints: molecular dynamics of n-alkanes. J Comput Phys 1977;23:327–341.

30. Humphrey W, Dalke A, Schulten K. VMD: visual molecular dynamics. J Mol Graph 1996;14:33–38,27–38.

31. Tripos. Sybyl 7.3. St. Louis, Missouri: Tripos; 1991–2008.

32. Accelrys. DS ViewerPro Suite 6.0. San Diego, CA: Accelrys; 2005.

33. Case D, Darden T, Cheatham TI, Simmerling C, Wang J, Duke R, Luo R, Crowley M, Walker R, Zhang W, Merz K, Wang B, Hayik S, Roitberg A, Seabra G, Kolossváry I, Wong K, Paesani F, Vanicek J, Wu X, Brozell S, Steinbrecher T, Gohlke H, Yang L, Tan C, Mongan J, Hornak V, Cui G, Mathews D, Seetin M, Sagui C, Babin V, Kollman P. AMBER 10. San Francisco: University of California, CA; 2008.

34. Onufriev A, Bashford D, Case DA. Exploring protein native states and large-scale conformational changes with a modified generalized born model. Proteins 2004;55:383–394.

35. Sitkoff D, Lockhart DJ, Sharp KA, Honig B. Calculation of electrostatic effects at the amino terminus of an α-helix. Biophys J 1994;67:2251–2260.

36. Bombarda E, Ullmann GM. pH-dependent pK_a values in proteins—a theoretical analysis of protonation energies with practical consequences for enzymatic reactions. J Phys Chem B 2010;114:1994–2003.

37. Gorecki A, Szypowski M, Dlugosz M, Trylska J. RedMD—reduced molecular dynamics package. J Comput Chem 2009;30:2364–2373.

38. Mueller DS, Kampmann T, Yennamalli R, Young PR, Kobe B, Mark AE. Histidine protonation and the activation of viral fusion proteins. Biochem Soc Trans 2008;36:43–45.

39. Li Y, Drone C, Sat E, Ghosh HP. Mutational analysis of the vesicular stomatitis virus glycoprotein G for membrane fusion domains. J Virol 1993;67:4070–4077.

40. Shokralla S, He Y, Wanas E, Ghosh HP. Mutations in a carboxy-terminal region of vesicular stomatitis virus glycoprotein G that affect membrane fusion activity. Virology 1998;242:39–50.

41. Nelson S, Poddar S, Lin TY, Pierson TC. Protonation of individual histidine residues is not required for the pH-dependent entry of west Nile virus: evaluation of the "histidine switch" hypothesis. J Virol 2009;83:12631–12635.

42. Cui Q, Li G, Ma J, Karplus M. A normal mode analysis of structural plasticity in the biomolecular motor F(1)-ATPase. J Mol Biol 2004;340:345–372.

43. Kleinekathofer U, Isralewitz B, Dittrich M, Schulten K. Domain motion of individual F(1)-ATPase βeta-subunits during unbiased molecular dynamics simulations. J Phys Chem A 2011;115:7267–7274.

44. Gaudin Y, Raux H, Flamand A, Ruigrok RW. Identification of amino acids controlling the low-pH-induced conformational change of rabies virus glycoprotein. J Virol 1996;70:7371–7378.